

Characterization of dendrite morphologies in rapidly solidified Al-4.5wt.%Cu droplets

M. Bedel¹, G. Reinhart¹, A.-A. Bogno², Ch.-A. Gandin³, S. Jacomet³, E. Boller⁴, H. Nguyen-Thi¹, H. Henein²

¹ Aix-Marseille University & CNRS, IM2NP UMR 7334, Campus Saint-Jérôme, Case 142, 13397 Marseille Cedex 20, France

² AMPL, Department of Chemical and Materials Engineering, University of Alberta, Canada

³ MINES ParisTech & CNRS, CEMEF UMR 7635, 06904 Sophia Antipolis, France

⁴ ESRF – The European Synchrotron, CS 40220, 38043 Grenoble Cedex 9, France

E-mail: marie.bedel@im2np.fr

Keywords: Rapid solidification, impulse atomization, synchrotron X-ray micro-tomography, Electron backscattered diffraction, dendrite morphology

Abstract

The Impulse Atomization process developed at the University of Alberta (Canada) enables metallic powders to be solidified with well controlled process parameters. The inner microstructure of several droplets of Al-4.5wt.%Cu alloy produced by this technique has been investigated by using both synchrotron X-ray micro-tomography and electron backscattered diffraction (EBSD). The 3D reconstructions obtained by micro-tomography are used to visualize cross sections of the droplets in any spacial directions. A wide range of dendrite morphologies are observed for different droplets of similar diameter and produced in the same

batch. Microstructural features indicate that the development of the dendrite arms (primary and of higher orders) occurs in most droplets along $\langle 111 \rangle$ crystallographic axes. This was unexpected as $\langle 100 \rangle$ directions are observed in conventional casting technologies. EBSD measurements were carried out on a selection of representative droplets after their characterization by synchrotron X-ray micro-tomography. Results confirm that most of the droplets are single grains and the relationship between the dendrite growth directions and the crystal orientation is determined unambiguously. Moreover, the large number of droplets analyzed by micro-tomography enabled a statistical analysis of the dendrite morphology as a function of droplet size and cooling atmosphere. The impact of different processing parameters on the final distribution of dendrite morphologies is also discussed.

1. Introduction

Rapid solidification techniques have been extensively developed in the last decades as they enable original microstructural and constitutional features to be obtained in the final products. Indeed, the large deviations from thermodynamic equilibrium induced by rapid solidification significantly alter the solidification conditions compared to those obtained at or close to equilibrium. The final properties can be modified through e.g. microstructure morphology change [1], extended solute solubility [2], non-equilibrium phases formation [2] or structure refinement [3]. The resulting solidified structures often lead to improved properties such as higher toughness, higher hardness, better wear resistance, better fatigue resistance or improved corrosion resistance.

In order to achieve rapid solidification, two potentially combined approaches are possible: imposing a high degree of primary phase nucleation undercooling or a high cooling rate [4]. It has been shown that nucleation undercooling values as high as $0.3T_m$, where T_m is the melting temperature, can be reached during droplet solidification of pure metals [5].

Moreover, it is possible to reach very large cooling rates when the surface to volume ratio of the system is high enough and the system is in presence of a large heat sink [2]. Typically, the solidification is considered to be rapid when the cooling rate is larger than 10^3 K/s [6].

Since Duwez' experiment in 1960 when it was demonstrated that the production of a metastable phase occurred in a small droplet from which the heat was extracted rapidly [7], various rapid solidification techniques have been developed. These mainly differ by the means used to form the metal volume and to extract heat. A review made by Savage and Froes describes for example more than 25 rapid solidification techniques [8]. While techniques such as melt extrusion or melt extraction lead to the formation of a continuous liquid stream for the manufacturing of wire, filament or ribbon type product, atomization techniques are the most commonly used techniques to produce powders and spray formed products. In these techniques, the liquid metal is destabilized and disperses into fine droplets in a much colder medium where the droplets cool rapidly. Liquid metallic droplets can either impact on a substrate surface and adhere to form a layer, or solidify before reaching the substrate. In the last case, the resulting powders can later be packed by sintering or cold or hot pressing to form high performance objects for automotive or aerospace applications.

The various atomization processes differ by the mechanism by which the liquid metal is converted into small droplets. In twin fluid atomization, the liquid metal is impacted by a second fluid at a high velocity, causing the droplet formation [9]. This second fluid can be a liquid or a gas. Alloys sensitive to oxidation are preferentially gas atomized with an inert gas such as nitrogen or argon. However, the control of the size distribution and the shape of the droplets remains limited with this process. The impulse atomization (IA) technique was developed to enable the production of powders with less variability in the droplet features.

Droplets of various aluminum based alloys formed by IA have been characterized in previous studies using stereology calculations on metallographs and X-ray or neutron powder

diffraction to quantify the final phase fractions [10] [11] [12] [13]. Neutron diffraction results combined with an approximate coarsening model have been recently successfully used to estimate the average eutectic and primary phase nucleation undercooling in aluminum alloy droplets [14][15]. However, these characterization methods only provide average information, which can hide significant variability within the droplet population, for instance in the case of a range of nucleation undercooling or cooling rate, or due to recalescence within a single droplet. Preliminary investigations on Al-Cu alloys using synchrotron X-ray micro-tomography have shown that this technique can be extremely useful to provide extra information about the solidification features in 3D [16]. However, the solidification microstructures could not be analyzed in details for a large number of droplets at that time.

The aim of the present work is to present results of advanced characterization of a large number of Al-4.5wt.%Cu droplets formed by the IA technique [17]. Synchrotron X-ray micro-tomography has been conducted in conjunction with electron backscattered diffraction (EBSD) in order to characterize the microstructure of the droplets. The combination of these two techniques has already proven very efficient, for instance in the study of the dendrite orientation transition in Al-Zn alloys [18][19]. Through synchrotron X-ray micro-tomography, 3D reconstructions of a large number of droplets have been achieved, which enables for the first time the occurrence of different droplets morphologies to be statistically analyzed. Droplets for which the analysis of the tomography data highlights representative features have been selected and analyzed by EBSD in order to correlate the observed morphological and crystallographic information. Moreover, the impact on the microstructure morphology of parameters acting on the cooling rate, such as the droplet size or the nature of the cooling gas, is considered. From these analyses, an interpretation of the evolution of the morphology distribution as a function of process parameters is proposed.

2. Droplet production and characterization techniques

2.1. Droplet production

The Al-4.5wt.%Cu alloy is chosen for this study as it is a widely used model alloy for solidification studies. Moreover, its thermo-physical properties are well defined and former powder atomization studies have been carried out [20]. The investigated droplets were produced by the Impulse Atomization (IA) technique, developed at AMPL (Advanced Materials & Processing Laboratory, Edmonton, Canada) [17]. In this process, the alloy is melted in a furnace and then pushed by mechanical impulses through a nozzle plate containing orifices of a defined diameter. The formed liquid jets break down into small droplets due to the Plateau-Rayleigh instability. The droplets lose their heat and solidify while falling through a stagnant gas atmosphere of either argon or helium. They are fully solidified before reaching an oil quench bath placed 4 meters under the atomizing nozzle. This technique leads to a size distribution of the droplets, whose diameter may vary from less than 200 μm to more than 1 mm in the same batch. The solidified droplets are sieved into different size classes based on the technique described in [21]. More precisely, the droplets are separated into 10 size classes, from a class containing the droplets smaller than 212 μm in diameter to a class containing the droplets larger than 850 μm in diameter. The diameter range (in microns) of the 10 classes are as follows: [0-212], [212-250], [250-300], [300-355], [355-425], [425-500], [500-600], [600-710], [710-850] and [850-1000].

2.2. Synchrotron X-ray micro-tomography

Synchrotron X-ray micro-tomography [22] has been carried out post-mortem to investigate the microstructure of the droplets. This technique has the advantage of providing a 3D representation of the droplets without being destructive. Three campaigns performed at ESRF (European Synchrotron Radiation Facility, Grenoble, France) on the ID19 beamline enabled

an examination of a very large number of droplets. The procedure is illustrated in Figure 1. Several droplets of a given size range were introduced into a cylindrical glass capillary filled with epoxy resin to prevent them from moving during image acquisition. The scatter consists of rotations enabling 1000 radiographs to be recorded at different view angles [23]. The volume was reconstructed by using a filtered back projection algorithm, which generated a stack of transverse images for each scan. From the image acquisition and the volume reconstruction performed at ESRF, two kinds of images were obtained depending on the post-processing technique used for the volume reconstruction: the standard filtered back projection algorithm that provides images based on the difference in X-ray attenuation coefficient between the different phases in the droplet [24], and a reconstruction algorithm developed more recently from the work of Paganin et al. [25] based on phase retrieval. In both cases, the difference in grey level in the images is mainly due to the difference in density and composition between the primary phase (Al-rich, dark grey in Figure 1.b), the eutectic (mixture of Al-rich and Al₂Cu, light grey in Figure 1.b) and porosity (black pockets in the droplet in Figure 1.b). Thus, the primarily formed dendrites can be distinguished from the eutectic structure and porosity. The “Paganin” images are used thereafter in all the presented figures because they show a better contrast between the two phases. Two pixel resolutions were used: a high resolution of 0.18 μm/pixel (field of view of 369 μm side cube) to analyze in detail the fine microstructure of small droplets, and a medium resolution of 0.56 μm/pixel (field of view of 1146 μm side cube) to scan either the biggest droplets, or several small droplets at the same time to derive statistical data. Finally, the reconstructed volumes were analyzed by using ImageJ software [26]. As the final droplet microstructure is the result of a complex 3D competition between dendrite arms, we focused on studying cross sections showing characteristic morphologies after manually searching the data stacks, such as the dendritic plane shown in Figure 1.b. This was made possible because the synchrotron X-ray

micro-tomography reconstructions enable the selection of the images corresponding to a particular droplet and to rotate them in the three spatial directions to locate distinctive features.

2.3. Electron backscattered diffraction (EBSD)

After the analysis of the tomography data, 6 droplets showing representative inner microstructures were selected to be analyzed by EBSD at MINES ParisTech (Sophia Antipolis, France). Each droplet was carefully removed from the epoxy resin in the capillary glass container, fixed in a conductive resin and polished using increasingly fine emery papers. After a final emery paper polishing with 1 μm diamond powder, each sample was polished with a colloidal silica solution in a vibration table. Then, the texture of the resulting droplet cross section was analyzed by an automated EBSD system mounted in a FEI XL30 ESEM scanning electron microscope (SEM). The pseudo-Kikuchi lines produced by backscattered electrons are detected by a Silicon Intensified Target Camera and the orientation of a large number of points of the cross section (spatial resolution of 3 μm) is automatically determined. The three resulting Euler angles give the orientation with respect to a reference frame for each measured point of the cross section. The corresponding $\langle 100 \rangle$, $\langle 101 \rangle$ and $\langle 111 \rangle$ pole figures were reconstructed by considering the Euler angles of all the studied points. An example of such an analysis is given in Figure 2. The SEM image of the cross section shown in Figure 2.a corresponds to a droplet of diameter equal to 962 μm solidified in argon, as prepared for the EBSD measurement. The active cross section was scanned with the spatial resolution given above. The three pole figures obtained by EBSD are shown in Figure 2.c, with the color of each point corresponding to its orientation according to the color map of the inverse pole figure drawn in Figure 2.d.

The SEM cross sections were actually randomly selected because it was not possible to orient the droplets before their fixation in the conductive resin, nor precisely control the thickness of

removed material during the polishing step. It was nevertheless possible to find the corresponding images in the tomography data by searching for similar morphological features. For example, the tomography image in Figure 2.b was found to correspond to the SEM image of Figure 2.a. Once the SEM cross section is identified in the micro-tomography reconstruction, it is possible to associate any tomography plane and direction with a crystallographic orientation. As a consequence, a particular growth orientation that is identified in the 3D reconstruction by geometrical considerations can also be compared to the crystallographic orientation displayed in the three pole figures. This analysis method was applied to characterize the four distinct morphologies identified in the studied droplets that will be presented in the next section.

3. Results

3.1. Grain structure and position of the nucleation event

A total of 230 droplets of two size classes solidified in two gas atmospheres have been analyzed by synchrotron X-ray micro-tomography. Among those, 137 of the studied droplets were solidified in argon atmosphere (73 with diameter lower than 212 μm and 64 with diameter between 250 μm and 300 μm) and 98 droplets in helium atmosphere (62 with diameter lower than 212 μm and 36 with diameter between 250 μm and 300 μm). The detail of the studied droplets is given in Table 1. The analysis of the 3D reconstruction for each droplet enabled to clearly distinguish the primary dendrite arms. The location of the nucleation center was then identified as the intersection of the primary dendrite arms. Only one nucleation center was usually observed, while in some rare cases two grains were identified by the intersection of dendrite arms with no particular orientation link. Moreover, a very light grey region separating the two grains was observed, which corresponds to a eutectic-rich zone at the grain boundary. No more than two grains in one droplet were

observed in the 230 studied droplets and only 8 were composed of two grains, i.e. approximately 3.4% of all droplets (Table 1). The EBSD analyses confirmed the grains number deduction made by synchrotron X-ray micro-tomography on the 6 selected droplets: when the droplet was made of a single grain, a unique crystallographic orientation was found in EBSD, while two zones of distinct orientation were clearly distinguished when analyzing a cross section cutting the two grains of a single droplet. More precisely, a unique crystallographic orientation corresponds to a maximum of 4 spots in the $\langle 001 \rangle$ pole figure, 7 spots in the $\langle 101 \rangle$ pole figure and 6 spots in the $\langle 111 \rangle$ pole figure, with an almost uniform color. When the analyzed surface cuts two grains, an additional pattern of dots with a different color is observed.

In addition to the number of nucleation sites, synchrotron X-ray micro-tomography enabled to locate precisely the nucleation position in the droplet. The ratio between the distance R_{nuc} , corresponding to the distance between the droplet center and the nucleation center, and the average droplet radius R_{drop} was calculated for the 222 single grain droplets. The droplet center position had to be estimated first to calculate this ratio. An approximate initial position was manually imposed and the distance between this position and each point of the droplet surface was calculated, resulting in a radius distribution. By minimizing the standard deviation of the droplet radius distribution, it was possible to get both the droplet center position and the droplet mean radius. Thus, a ratio $R_{\text{nuc}} / R_{\text{drop}}$ close to 0 corresponds to a nucleation close to the droplet center while a ratio close to 1 corresponds to a nucleation close to the droplet surface. The distribution of the nucleation center position is given for two droplet diameter ranges, solidified in argon in Figure 3.a and in helium in Figure 3.b. It is visible that for the two used gas atmospheres, the nucleation position does not depend on the droplet size. Moreover, nucleation is observed to occur more preferentially close to the

surface in droplets solidified in argon atmosphere compared to droplets solidified in helium where the nucleation position is more evenly distributed.

These measured distributions are compared to the theoretical distribution of nucleation position in the case of an equiprobable nucleation in the volume. If the nucleation is random in a droplet, the probability to nucleate is the same in the whole droplet volume. The droplet volume between 0.9 and 1.0 of the normalized radius being larger than the volume between 0.0 and 0.1, this means that the probability to nucleate close to the surface is also higher. This theoretical distribution of nucleation position in the case of a random nucleation is given in Figure 3.a and Figure 3.b by the black diamonds. By comparing the experimentally determined distribution of nucleation position with the theoretical one, it can be seen that nucleation is actually random in droplets solidified in helium, as the experimental distribution of nucleation position is very close to the theoretical one for both size categories.

3.2. Dendrite growth morphologies

By identifying characteristic planes in the three-dimensional reconstructions of the droplets obtained by synchrotron X-ray micro-tomography, four typical dendrite morphologies have been distinguished in the 230 studied droplets. We intend to develop the characteristics of each of these morphologies in the following four sub-sections.

3.2.1. $\langle 100 \rangle$ highly branched microstructure

The first morphology is characterized by a highly branched dendritic microstructure. A representative cross section of such morphology is shown in Figure 4.a. The two red arrows highlight the position of two primary arm directions. From these arms, other arms grow orthogonally, which induces a grid pattern in three dimensions. A highly branched structure is observed close to the primary arms while further in the droplet the grid pattern becomes clearer. It is worth noting that a rotation of 90° around x or y axis from this characteristic

cross section leads to the observation of cross sections with similar morphology. This suggests that the whole dendrite microstructure develops along the usual $\langle 100 \rangle$ directions.

A droplet showing a highly branched structure and for which a 3D reconstruction existed was analyzed by EBSD in order to correlate the dendrite growth direction and the crystallographic orientation. By applying the procedure detailed in section 2.3, the pole figures in Figure 4.b related to the droplet cross section in Figure 4.a were obtained. The corresponding inverse pole figure is given in Figure 4.c and clearly shows that the whole cross section is contained in a $\{100\}$ plane. The primary directions highlighted by the red arrows in the cross section can be found back in the $\langle 100 \rangle$ pole figure. This observation is consistent with a growth direction along $\langle 100 \rangle$ axes as inferred from micro-tomography observations.

3.2.2. $\langle 111 \rangle$ to $\langle 100 \rangle$ transition microstructure

The second morphology is more complex. As for the previous morphology, synchrotron X-ray micro-tomography enabled to distinguish a highly branched microstructure far from the nucleation center. However, the microstructure close to the nucleation center is different. In this case, eight primary arms appearing as straight dark lines in the tomography reconstructions and crossing in a single point (identified as the nucleation center) were observed. Furthermore, the angle between two arms was found to be close to 70° . As this value does not correspond to the 90° relationship between two arms observed in the case of a $\langle 100 \rangle$ growth direction, it results that the arms did not developed along $\langle 100 \rangle$ crystallographic axes. Moreover, a third arm can be found from a plane containing two primary arms by applying a rotation of 120° around one arm in the 3D reconstruction. In all the analyzed droplets, this rotation of 120° when looking for another arm is almost perfectly respected and no more than a 3° deviation is found. The latter two angles are actually coherent with a growth of the primary arms along $\langle 111 \rangle$ axes. Indeed, for this growth orientation, the theoretical angle between two primary arms would be equal to 70.5° and the angle between

planes containing primary arms equal to 120° , which is in agreement with the previous measurements. Therefore droplets of this type grow in $\langle 111 \rangle$ directions at first. As far from the nucleation center, a $\langle 100 \rangle$ growth orientation is observed, a transition of growth orientation direction from $\langle 111 \rangle$ to $\langle 100 \rangle$ must occur during the solidification of this type of droplets.

These geometrical observations made on a large number of droplets by analyzing their 3D reconstruction have been confirmed by the EBSD analysis of a droplet with a diameter of $510 \mu\text{m}$ solidified in argon and showing this particular microstructure, as illustrated in Figure 5 to Figure 7. Figure 5 shows a 3D schematic view of the droplet, with the nucleation center given by a white dot and the $\langle 111 \rangle$ primary arms highlighted by blue arrows. The green plane corresponds to the $\{101\}$ cross section analyzed in Figure 6 and the red plane corresponds to the $\{001\}$ plane analyzed in Figure 7.

Indeed, the micro-tomography cross section given in Figure 6.a shows the $\{110\}$ plane containing two primary arms (highlighted by two blue arrows) reported in green in the 3D schematic Figure 5. The corresponding pole figures and inverse pole figure are given in Figure 6.b and Figure 6.c. Among the four $\langle 111 \rangle$ directions, only the two directions directed toward the left-hand part of the $\langle 111 \rangle$ pole figure in Figure 6.b correspond to the growth direction of the two primary arms shown in Figure 6.a. The two other $\langle 111 \rangle$ directions are not found in the micro-tomography data due to the nucleation location at the droplet surface.

The other analyzed cross section, corresponding to the red plane in Figure 5, is shown in Figure 7.a. It was obtained by applying a 45° rotation around y axis to the cross section of Figure 6.a and going away from the nucleation center position. We can note that, by this rotation, one passes from a cube diagonal plane (corresponding to a $\{101\}$ plane containing four $\langle 111 \rangle$ directions) to a cube face (corresponding to a $\{100\}$ plane). A highly branched pattern is observed, as previously shown in Figure 4.a. The pole figures and inverse pole

figure corresponding to this new cross section are given in Figure 7.b and Figure 7.c. They show that the cross section belongs to a $\{100\}$ crystallographic plane and that $\langle 100 \rangle$ directions are directed horizontally and vertically. Therefore, the usual $\langle 100 \rangle$ growth orientation is found back in this region of the droplet. Thus, the micro-tomography analyses completed by EBSD measurements unambiguously highlight a growth orientation transition in this droplet from a $\langle 111 \rangle$ primary arms growth orientation to a $\langle 100 \rangle$ growth orientation of the last formed solid. The highly complex and fine dendrite features in the intermediate region do not enable to detail the transition between those two growth orientation regions, even with the highest spatial resolution used.

3.2.3. $\langle 111 \rangle$ dendritic morphology

The third identified morphology is illustrated in Figure 8.a, where a characteristic cross section of a 255 μm diameter droplet solidified in argon is shown. In the droplets with this type of characteristic planes, eight primary arms directed towards the eight $\langle 111 \rangle$ directions were found (when the nucleation does not occur at the droplet surface), in the same way as the primary arms in the second dendrite morphology described previously in paragraph 3.2.2. However, the characteristic cross sections containing two primary arms are different. Instead of the fine structure observed between primary arms for the second type of morphology (as seen in Figure 6.a), a clear network of dendritic arms is visible. Secondary, tertiary and higher order arms developed in the cross section from the primary arms. The angle between two primary arms is approximately 70° , which is consistent with a growth along $\langle 111 \rangle$ axes. Similarly, the secondary arms make a 70° angle with the primary arms, the tertiary arms make a 70° angle with the secondary arms and so on for higher arm orders. This type of microstructure is found in the six cross sections containing two primary arms and making a 120° angle between each other. This configuration is shown in three dimensions in Figure 8.b where the characteristic cross section shown in Figure 8.a as well as the other five

characteristic cross sections of the droplet are reported. The nucleation center is placed at the center of a cube, with the eight primary arms pointing towards the cube corners as expected for a growth along $\langle 111 \rangle$ axes. Although the nucleation center is close to the droplet surface, the six dendritic cross sections were retrieved and the 3D pattern of the first solidified structures in the droplet is highlighted. The two primary arms highlighted by blue arrows in Figure 8.a, *A arm* and *B arm*, are identified in Figure 8.b. This type of dendrite morphology actually entirely fills the droplet in a complex dendritic network and these observations show that the whole droplet solidified with a dendritic microstructure growing in $\langle 111 \rangle$ directions. For this droplet category, a supplementary observation has to be considered. Indeed, two almost parallel dendritic planes apart from each other of few micrometers and coming from the nucleation center were found in the six primary directions for some of the droplets. An example of such a microstructure pattern is given in Figure 8.c, for a 244 μm diameter droplet solidified in argon. More precisely, 60% of the 58 droplets showing the third dendrite morphology actually grew such double planes.

3.2.4. $\langle 111 \rangle$ finger bundle morphology

Finally, Figure 9 and 10 show examples of the fourth dendrite morphology identified in this study. This morphology is characterized by a large number of primary arms originating from the nucleation center as can be distinguished in the cross sections shown in Figure 9.a or Figure 10.b. However, all the geometrical relationships between planes corresponding to a $\langle 111 \rangle$ oriented growth are found back in this type of droplets, and similar characteristic planes can be found by applying a rotation of 120° around the average growth direction of these arms. Moreover, partial dendritic planes can be found farther from the nucleation center, with the characteristic $\langle 111 \rangle$ growth morphology described in the previous paragraph 3.2.3. The poles figures in Figure 9.b are related to the droplet cross section shown in Figure 9.a. As in the second and third morphologies, the EBSD result shows that the cross section belongs to

a $\{101\}$ crystallographic plane and contains four $\langle 111 \rangle$ directions highlighted by the blue arrows. This observation is once again consistent with a fully $\langle 111 \rangle$ oriented growth.

The precise orientation of the characteristic cross sections is nevertheless more difficult to determine in droplets of this category from the micro-tomography data as a large number of arms with few branching expand from the nucleation center and grow in an almost parallel manner in three dimensions. A more detailed description of this complex morphology is provided in Figure 10 showing three cross sections of a 264 μm diameter droplet solidified in argon. Figure 10.b represents a $\{101\}$ plane showing the multiple arms developing in the $\langle 111 \rangle$ directions and corresponds to the green plane A in the 3D schematic given in Figure 10.a. Figure 10.c and Figure 10.d are $\{111\}$ parallel planes orthogonal to a primary arm direction. They correspond to the blue planes B and C in Figure 10.a. Plane B is taken close to the nucleation center while plane C is taken farther in the droplet. Those cross sections highlight the 120° angle between the three characteristic planes passing by one primary arm. Moreover, they show a widening of the region containing multiple arms starting from the nucleation center and developing around the $\langle 111 \rangle$ direction. This region consists in an almost triangular zone made of small circular structures. It corresponds to the cross section of the bundle of arms and is highlighted by the blue triangles. As the bundle enlarges while solidifying, the triangle gets larger while going farther from the nucleation center (e.g. from plane A to plane B). To our knowledge, such a microstructure has not been reported before and it will thereafter be termed *finger bundle* morphology.

3.3. Dendrite morphology distribution as a function of process parameters

Synchrotron X-ray micro-tomography enables the morphology characterization of a large number of droplets as well as the correlation of this information with process parameters and droplet properties. As specified in paragraph 2.1, atomization experiments were performed with argon and helium gases and the resulting droplets were sieved in size range categories.

Therefore, the distribution of the four morphologies can be quantified as a function of the two size categories studied hereby and the two used cooling gases. The dendrite morphology distribution is shown for the two size categories of droplets solidified in argon in Figure 11.a and in helium in Figure 11.b. 73 droplets smaller than 212 μm in diameter and 64 droplets with diameter between 250 μm and 300 μm are considered with cooling in argon gas. 62 droplets smaller than 212 μm in diameter and 31 with diameter between 250 μm and 300 μm are considered with cooling in helium (Table 1).

The four morphologies are found in droplets solidified in argon with a diameter between 250 μm and 300 μm as can be seen in Figure 11.a. Therefore; the dendrite morphology is not unique to a droplet size category. However, by comparing the morphology distribution for the two sizes, it is observed that the morphology tends to be more often of the <111> finger bundle type when the droplet size decreases. This observation remains true for droplets solidified in helium atmosphere, as can be seen in Figure 11.b. The effect of the cooling gas can be pointed out by comparing Figure 11.a and Figure 11.b. For the same size category, the morphology is more often of the finger bundle type in droplets solidified in helium.

4. Discussion

The analysis of synchrotron X-ray micro-tomography data enabled to determine the number of grains formed in droplets. Most of the droplets are single grains (regardless of the cooling gas) and this was confirmed for some droplets by EBSD. Micro-tomography analyses also enabled to go further as the position of the nucleation event(s) was localized in each studied droplet. As seen in Figure 3, the droplet size does not seem to have a significant effect on the nucleation position. However, a clear impact of the cooling gas is observed. The randomly distributed nucleation position determined for helium cooled droplets is replaced by a preferential surface nucleation in argon cooled droplets.

The effect of the cooling gas on nucleation can be either direct through chemical interactions with the droplet surface or indirect through heat extraction from the droplet. In order to estimate the heat extraction rate from the droplet towards the surrounding gas, the temperature is usually considered uniform in the whole droplet. This hypothesis commonly made under the condition of a small droplet is not obvious as the Biot number, characteristic of the ratio between heat transfer inside the droplet and at its surface, does not depend only on the droplet size. For a droplet of a given diameter and a given alloy, it also depends on the heat transfer coefficient at the interface and therefore on the surrounding gas. This coefficient is difficult to estimate as the droplet is falling, and possibly rolling, during solidification, which induces gas flow around it. The isothermal assumption made in most of the atomization process analyses is coherent with the random nucleation position observed in helium cooled droplets. A non-isothermal flow hypothesis made on a droplet solidification model even showed that the temperature can be considered as uniform in the droplet, except just after nucleation [27]. Therefore the temperature uniformity hypothesis seems valid before nucleation. However, it does not enable the preferential nucleation position at the surface for argon cooled droplets to be explained. Other phenomena should be considered to explain the nucleation position at the surface in almost all the droplets cooled in argon.

The droplet analysis by combining synchrotron X-ray micro-tomography and EBSD also provided original information about the micro-structure morphology. The growth directions identified in droplets by micro-tomography have been compared to the crystallographic orientation of cross sections given by EBSD. The two techniques converge to indicate that the dendritic structures grow along characteristic crystallographic directions. However, only 18 droplets out of 230 whose morphology is analyzed by X-ray micro-tomography, i.e. 7.8%, show a full $\langle 100 \rangle$ growth orientation (Table 1). The remaining droplets present (at least partially) less usual $\langle 111 \rangle$ grown structures. The aluminum-copper alloy is indeed commonly

considered to grow in $\langle 100 \rangle$ directions [28], as for the face-centered cubic (fcc) structures in general [29].

Growth direction changes in fcc crystals have already been reported experimentally. Kahlweit et al. highlighted the growth orientation change of $\text{NH}_4\text{Cl-H}_2\text{O}$ crystals from $\langle 100 \rangle$ to $\langle 110 \rangle$ and then $\langle 111 \rangle$ with increasing growth velocity [30]. The authors investigated the growth orientation by varying the nucleation undercooling through solute composition and solidification temperature. Chan et al. suggested that, at low undercooling, the growth orientation is imposed by the anisotropy of interfacial free energy, while at high undercooling it is controlled by the “anisotropy of rate constant” [31]. By directionally solidifying this alloy, oscillations between these different growth modes were also seen by Gudgel et al. [32]. On the other hand, the investigation of Haxhimali et al. [33] on the dendrite growth orientation of directionally solidified Al-Zn alloys showed a change from $\langle 100 \rangle$ to $\langle 110 \rangle$ for a range of solute compositions. The latter result being independent of the solidification velocity, the authors concluded that the continuous orientation change is due to anisotropy variation of the surface energy and not to attachment kinetics anisotropy for this dendrite orientation transition. Using EBSD analysis, Chen et al. showed that a textured structure with a preference in the $\langle 111 \rangle$ direction was observed in Al-0.6wt.%Fe and Al-1.9wt.%Fe atomized using IA [34]. In the same way, Castle et al. recently reported a number of morphological transitions with increasing undercooling for a Cu-Ni alloy, interpreted as an extended transition between fully $\langle 100 \rangle$ and $\langle 111 \rangle$ growth orientations [35]. All these experiments suggest that the variation of interfacial energy anisotropy can induce a $\langle 100 \rangle$ to $\langle 110 \rangle$ transition, while the attachment kinetics anisotropy variation would explain the $\langle 111 \rangle$ orientation outbreak, with the transition to $\langle 111 \rangle$ growth linked to the solidification rate.

This interpretation is coherent with our observations. Indeed, the solute composition and the process parameters being imposed, a distribution of the solidification growth velocity in the

droplets can be the reason for the reported growth morphology distribution. As described in paragraph 3.2.1, the growth orientation is $\langle 100 \rangle$ in highly branched droplets (Figure 4) and we therefore can suppose that they formed at the slowest velocity. Then, for higher cooling rate, the primary arms would start growing in $\langle 111 \rangle$ directions but the higher level arms that solidify later and more slowly after recalescence would grow in $\langle 100 \rangle$ directions. This corresponds to the second morphology shown in Figure 5 to Figure 7. Then, when the cooling rate is even higher, the growth orientation remains $\langle 111 \rangle$ in the whole droplet as illustrated in Figure 8. Finally, for the fastest velocities, the competition between several primary arms growing in the $\langle 111 \rangle$ direction leads to the finger bundle morphology observed in Figure 9 and Figure 10. The $\langle 111 \rangle$ dendritic structure is found back in regions of the droplet with slower solidification velocity. These results show that a range of solidification rate may be obtained in the IA production of droplets, even for imposed process conditions and for a given droplet size. The origin of the solidification velocity range can be the local thermal interactions between the droplets or a distribution of nucleation undercooling. This distribution would be large enough to induce a morphology distribution, from highly branched to finger bundle, passing by highly branched with visible primary arms and dendritic morphologies.

In addition, the effect of the cooling gas and the droplet size confirms the relationship between the dendrite morphology and the solidification velocity. Indeed, when the droplet is smaller, the surface to volume ratio of the droplet increases. All other parameters considered identical, the cooling rate and therefore the averaged solidification velocity are faster. This is confirmed by secondary dendrite arm spacing measurements made on characteristic planes of $\langle 111 \rangle$ dendritic droplets. This parameter, which characterizes the local solidification velocity, has been estimated in 21 argon cooled droplets. For each of these droplets, the distance between two consecutive secondary dendrite arms is evaluated in a characteristic plane, in

addition to the average diameter estimation from the 3D tomography reconstruction. A clear tendency can be extracted from these measurements. For a diameter between 135 μm and 293 μm , the average SDAS (secondary dendrite arm spacing) varies from 6.4 μm to 9.4 μm . Despite some small fluctuations induced by the measurement technique, a clear SDAS increase is observed when the droplet diameter increases, which indicates that smaller droplets solidify faster. The effect of droplet size on the morphology proportion illustrated in Figure 11.a is coherent with the previous observation. When the droplets are smaller, they solidify faster hence the observed growth orientation tends to be more $\langle 111 \rangle$ and more droplets with finger bundle dendrites are obtained.

Similar conclusions can be drawn regarding the impact of the cooling gas. The thermal conductivity of helium is more than 8 times larger than the one of argon. Therefore, the heat extraction is much faster for droplets solidified in helium than in argon atmosphere. This is again found back in the SDAS measurements made on $\langle 111 \rangle$ dendritic droplets of similar diameter solidified in the two different gas atmospheres. The average SDAS varies from 7.5 μm in argon cooled droplets to 4.0 μm in helium cooled droplets, for droplets with an average diameter of 200 μm ($\pm 10 \mu\text{m}$). Thus, droplets cooled in helium solidify faster and a larger proportion of dendrite structures with the $\langle 111 \rangle$ finger bundle morphology than in argon cooled droplets is obtained for a given size range. In summary, processing parameters such as the cooling gas nature and the droplet size have a significant impact on the average solidification velocity of the droplets and indirectly alter the dendrite morphology proportions.

5. Conclusion

The inner microstructure of a large number of Al-4.5wt.%Cu droplets formed by IA process has been studied by combining synchrotron X-ray micro-tomography and EBSD. The number of grains as well as the nucleation position in droplets was quantified. The determination of the nucleation position in droplets highlighted that most of the droplets are made of a single grain and that the nucleation occurs preferentially close to the surface in argon cooled droplets while it is random in the volume for helium cooled droplets.

The growth orientation of the microstructures has been linked with the crystallographic orientation of the grains. The determination of characteristic cross sections leads to the identification of four different morphologies for droplets of roughly the same size and formed under the same process conditions. These morphologies have been described in detail and a $\langle 111 \rangle$ growth orientation was highlighted. The existence of four distinct morphologies is attributed to a range of solidification velocity for droplets of the same batch. This is confirmed by analyzing the correlation between the different process parameters on both the solidification velocity (through SDAS measurements) and the morphology distribution.

The methodology used in this study enabled to carry out a detailed investigation of rapidly solidified droplets formed during the IA process. These results will be compared in the future with numerical simulations to investigate the effect of the thermal field on the nucleation position. Phase field modeling is also being considered to directly link the dendrite growth direction in a droplet to its solidification velocity. Indeed, if this study enabled us to get some innovative information about the dendrites morphology in rapidly solidified droplets, the understanding of the physical mechanism responsible for the $\langle 111 \rangle$ to $\langle 100 \rangle$ transition is still very limited. Consequently, modeling may be the most promising approach to study this phenomenon.

Acknowledgements

This study has been performed in the framework of the MIMOSA project funded by the French National Research Agency (ANR), by the Natural Sciences and Engineering Research Council (NSERC) of Canada and by Novelis. The authors are grateful to Barbara Fayard and Olivier Guiraud from Novitom for their technical support during the ESRF experiments and the reconstruction of the micro-tomography data. The authors would also like to thank Bernard Billia for fruitful discussions.

References

- [1] Boettinger W J, Bendersky L and Early J G 1986 An analysis of the microstructure of rapidly solidified Al-8 wt pct Fe powder *Metall. Trans. A* **17** 781–90
- [2] Sudarshan T S and Srivatsan T S 1993 *Rapid Solidification Technology: An Engineering Guide* (CRC Press)
- [3] Hatch J E 1984 *Aluminum: Properties and Physical Metallurgy* (ASM International)
- [4] Lewis R E, Palmer I G, Ekvall J C, Sakata I F and Quist W E 1983 Aerospace Structural Applications of Rapidly Solidified Aluminum-Lithium Alloys *Proc. Third Int. Conf. Rapid Solidif. Process.*
- [5] Holloman J H and Turnbull D 1951 Solidification of lead-tin alloy droplets *J. Met.* 35
- [6] Flemings M C, Tien J K and Elliot J F 1981 *Metall. Treatises Metall. Soc. AIME* 291–300
- [7] Duwez P, Willens R H and Klement W 1960 Continuous Series of Metastable Solid Solutions in Silver-Copper Alloys *J. Appl. Phys.* **31** 1136
- [8] Savage S J and Froes F H 1984 Production of rapidly solidified metals and alloys *J. Met.* 20–33
- [9] Lawley A 1977 An overview of powder atomization processes and fundamentals *Int. J. Powder Metall.* 169–88
- [10] Prasad A, Henein H, Maire E and Gandin C-A 2006 Understanding the rapid solidification of Al-4.3Cu and Al-17Cu using X-ray tomography *Metall. Mater. Trans. A* **37** 249–57

- [11] Henein H, Buchoud V, Schmidt R-R, Watt C, Malakov D, Gandin C-A, Lesoult G and Uhlenwinkel V 2010 Droplet Solidification of Impulse Atomized Al-0.61Fe and Al-1.9Fe *Can. Metall. Q.* **49** 275–92
- [12] Ilbagi A, Henein H and Phillion A B 2011 Phase quantification of impulse atomized Al68.5Ni31.5 alloy *J. Mater. Sci.* **46** 6235–42
- [13] Ilbagi A, Delshad Khatibi P, Swainson I P, Reinhart G and Henein H 2011 Microstructural analysis of rapidly solidified aluminium–nickel alloys *Can. Metall. Q.* **50** 295–302
- [14] Bogno A-A, Delshad Khatibi P, Henein H and Gandin C-A 2013 Quantification of primary dendritic and secondary eutectic undercoolings of rapidly solidified Al-Cu droplets *Materials Science & Technology 2013* vol 2 (Montreal, QC, Canada) pp 1153–60
- [15] Tourret D, Reinhart G, Gandin C-A, Iles G N, Dahlborg U, Calvo-Dahlborg M and Bao C M 2011 Gas atomization of Al–Ni powders: Solidification modeling and neutron diffraction analysis *Acta Mater.* **59** 6658–69
- [16] Prasad A, Mosbah S, Henein H and Gandin C-A 2009 A Solidification Model for Atomization *ISIJ Int.* **49** 992–9
- [17] Henein H 2002 Single fluid atomization through the application of impulses to a melt *Mater. Sci. Eng. A* **326** 92–100
- [18] Friedli J, Fife J L, Napoli P D and Rappaz M 2012 X-ray tomographic microscopy analysis of the dendrite orientation transition in Al-Zn *IOP Conf. Ser. Mater. Sci. Eng.* **33** 012034
- [19] Friedli J, Fife J L, Napoli P D and Rappaz M 2013 Dendritic Growth Morphologies in Al-Zn Alloys—Part I: X-ray Tomographic Microscopy *Metall. Mater. Trans. A* **44** 5522–31
- [20] Wiskel J B, Henein H and Maire E 2002 Solidification Study of Aluminum Alloys using Impulse Atomization: Part I: Heat Transfer Analysis of an Atomized Droplet *Can. Metall. Q.* **41** 97–110
- [21] Federation M P I 2012 *Standard Test Methods for Metal Powders and Powder Metallurgy Products 2012* (S.I.: Metal Powder Industry)
- [22] Nguyen-Thi H, Salvo L, Mathiesen R H, Arnberg L, Billia B, Suéry M and Reinhart G 2012 On the interest of synchrotron X-ray imaging for the study of solidification in metallic alloys *Comptes Rendus Phys.* **13** 237–45
- [23] Salvo L, Suéry M, Marmottant A, Limodin N and Bernard D 2010 3D imaging in material science: Application of X-ray tomography *Comptes Rendus Phys.* **11** 641–9
- [24] Kak A C and Slaney M 1988 Principles of computerized tomographic imaging IEEE (New York)

- [25] Nugent K A, Gureyev T E, Cookson D F, Paganin D and Barnea Z 1996 Quantitative Phase Imaging Using Hard X Rays *Phys. Rev. Lett.* **77** 2961–4
- [26] Abramoff M D, Magalhães P J and Ram S J 2004 Image processing with ImageJ *Biophotonics Int.* **11** 36–42
- [27] Heringer R, Gandin C-A, Lesoult G and Henein H 2006 Atomized droplet solidification as an equiaxed growth model *Acta Mater.* **54** 4427–40
- [28] Kato H and Umeda T 1978 Growth structures of Al-4.5 wt pct Cu alloys with dendrite growth directions differing from the heat flow direction *Metall. Trans. A* **9** 1795–800
- [29] Dantzig J A and Rappaz M 2009 *Solidification* (EPFL Press)
- [30] Kahlweit M 1970 On the dendritic growth of NH₄Cl crystals from aqueous solutions. II *J. Cryst. Growth* **7** 74–8
- [31] Chan S-K, Reimer H-H and Kahlweit M 1976 On the stationary growth shapes of NH₄Cl dendrites *J. Cryst. Growth* **32** 303–15
- [32] Gudgel K A and Jackson K A 2001 Oscillatory growth of directionally solidified ammonium chloride dendrites *J. Cryst. Growth* **225** 264–7
- [33] Haxhimali T, Karma A, Gonzales F and Rappaz M 2006 Orientation selection in dendritic evolution *Nat. Mater.* **5** 660–4
- [34] Chen J, Dahlborg U, Bao C M, Calvo-Dahlborg M and Henein H 2011 Microstructure Evolution of Atomized Al-0.61 wt pct Fe and Al-1.90 wt pct Fe Alloys - Springer *Metall. Mater. Trans. B* 1–11
- [35] Castle E G, Mullis A M and Cochrane R F 2014 Evidence for an extensive, undercooling-mediated transition in growth orientation, and novel dendritic seaweed microstructures in Cu–8.9 wt.% Ni *Acta Mater.* **66** 378–87

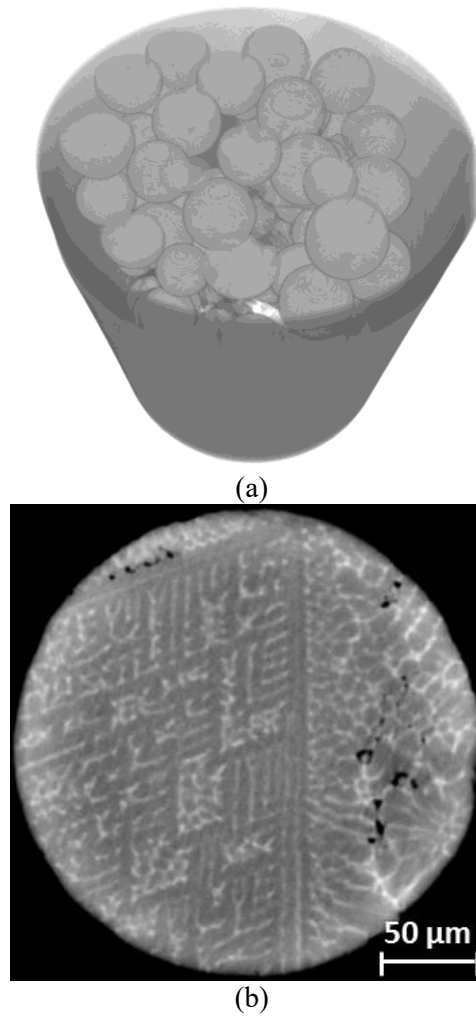


Figure 1. Example of synchrotron X-ray micro-tomography result: (a) three-dimensional reconstruction of a capillary containing droplets and (b) specific cross section in a selected droplet showing a $\langle 111 \rangle$ dendritic structure.

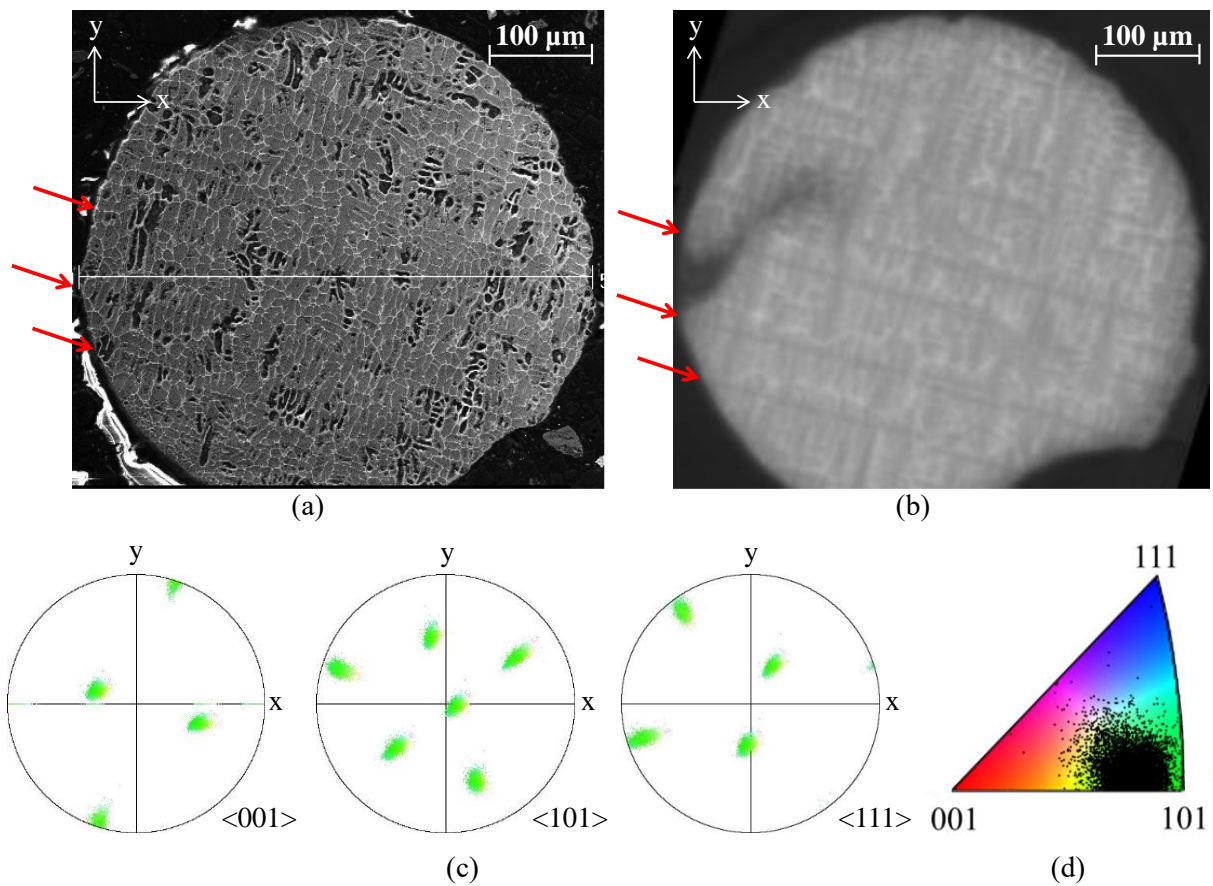
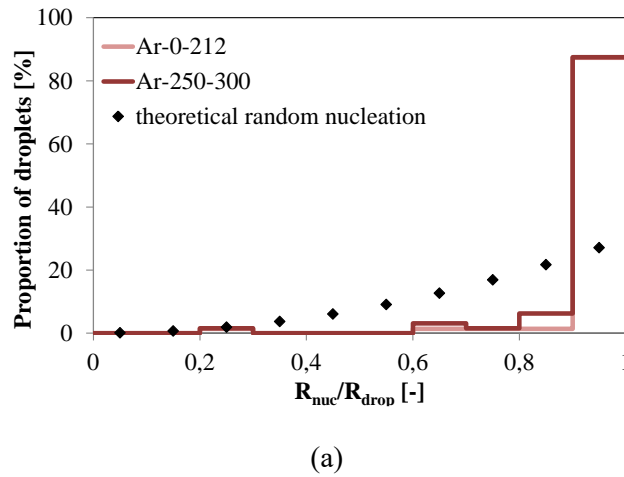


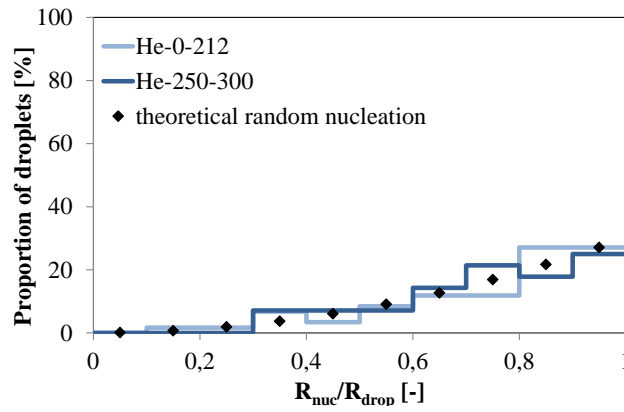
Figure 2. Example of EBSD result obtained for a 962 μm diameter droplet solidified in argon: (a) SEM image of a cross section, (b) corresponding plane retrieved from 3D reconstruction of the droplet by tomography, (c) corresponding $\langle 001 \rangle$, $\langle 101 \rangle$ and $\langle 111 \rangle$ pole figures and (d) inverse pole figure giving the orientation of each surface point. The red arrows highlight characteristic features used to identify the SEM cross section in the tomography reconstruction.

Cooling gas	Ar		He	
Droplet diameter [μm]	0 212	250 300	0 212	250 300
Total number of droplets	73	64	62	31
Number of single grain droplets	71	64	59	28
Number of droplets with <100> highly branched structures	5	12	0	1

Table 1. Number of droplets with <100> highly branched structures, number of single grain droplets and total number of droplets analyzed by X-ray micro-tomography, as a function of the droplet size range and cooling gas.



(a)



(b)

Figure 3. Characterization of the nucleation position in the droplets by tomography, considering the ratio between R_{nuc} , the distance between the droplet center and the nucleation center, and R_{drop} , the average droplet radius, for two droplets size ranges and for droplets solidified in (a) argon and (b) helium. A ratio close to 1 refers to a nucleation center close to the droplet surface and a ratio close to 0 to a nucleation center close to the droplet center. The distribution of the nucleation center position is shown for droplets of diameter smaller than 212 μm , 71 solidified in argon and 59 in helium, and for droplets of diameter between 250 μm and 300 μm , 64 solidified in argon and 28 in helium. The black dots correspond to the theoretical distribution of the nucleation center position if the nucleation is random in the droplet.

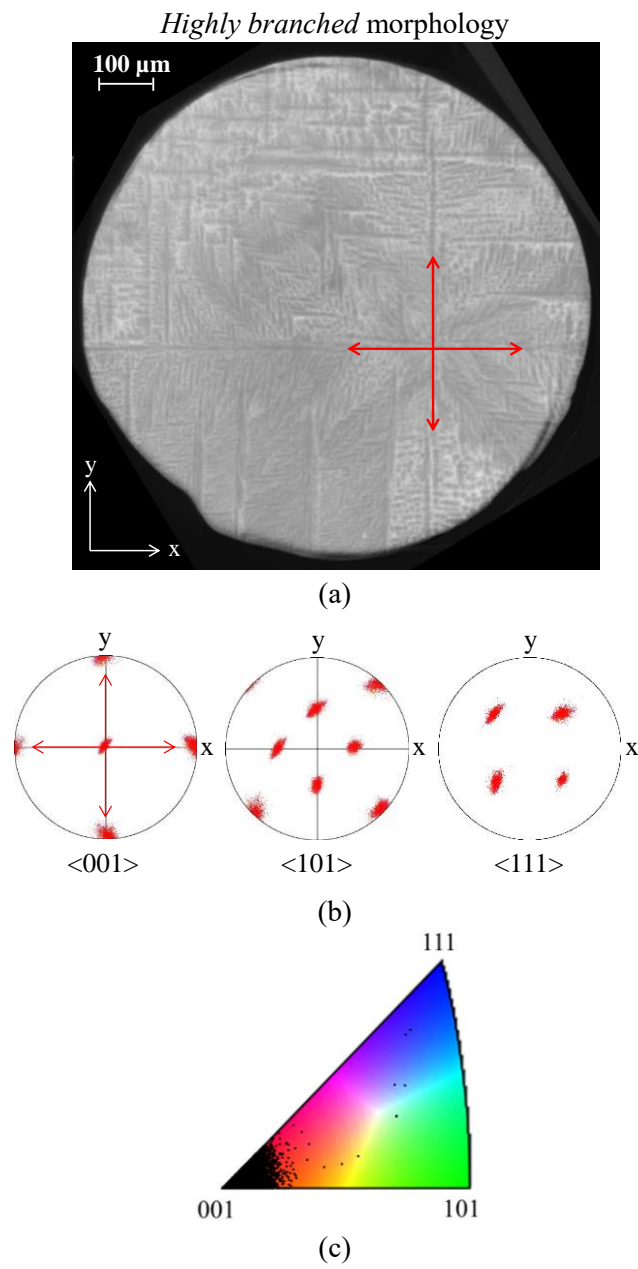


Figure 4. (a) Characteristic plane found in the tomography of a 960 μm diameter droplet solidified in argon showing a highly branched structure, and the corresponding (b) $\langle 001 \rangle$, $\langle 101 \rangle$ and $\langle 111 \rangle$ pole figures and (c) the inverse pole figure obtained by EBSD.

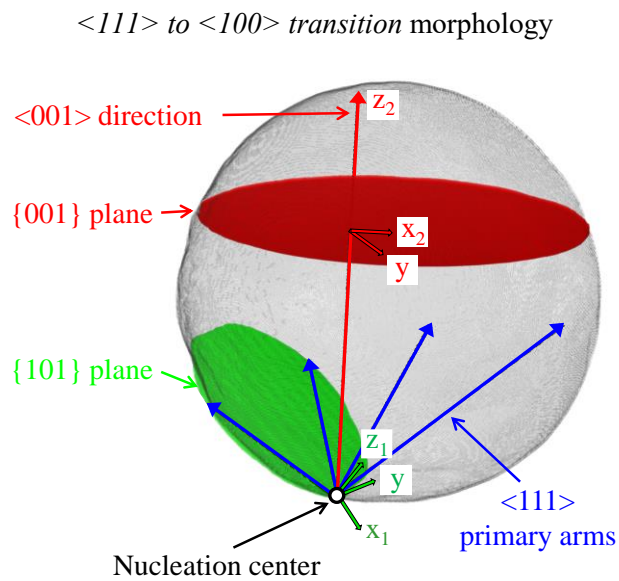


Figure 5. 3D schematic view of a 510 μm diameter droplet solidified in argon showing a $\langle 111 \rangle$ to $\langle 100 \rangle$ growth orientation transition, for which both tomography and EBSD analysis were realized. The four $\langle 111 \rangle$ primary arms directions are given by the blue arrows and a $\langle 001 \rangle$ direction is given by the red arrow. The primary arms converge at the nucleation center position given by the white dot. The green plane corresponds to a $\{101\}$ cross section and the red plane corresponds to a $\{001\}$ cross section.

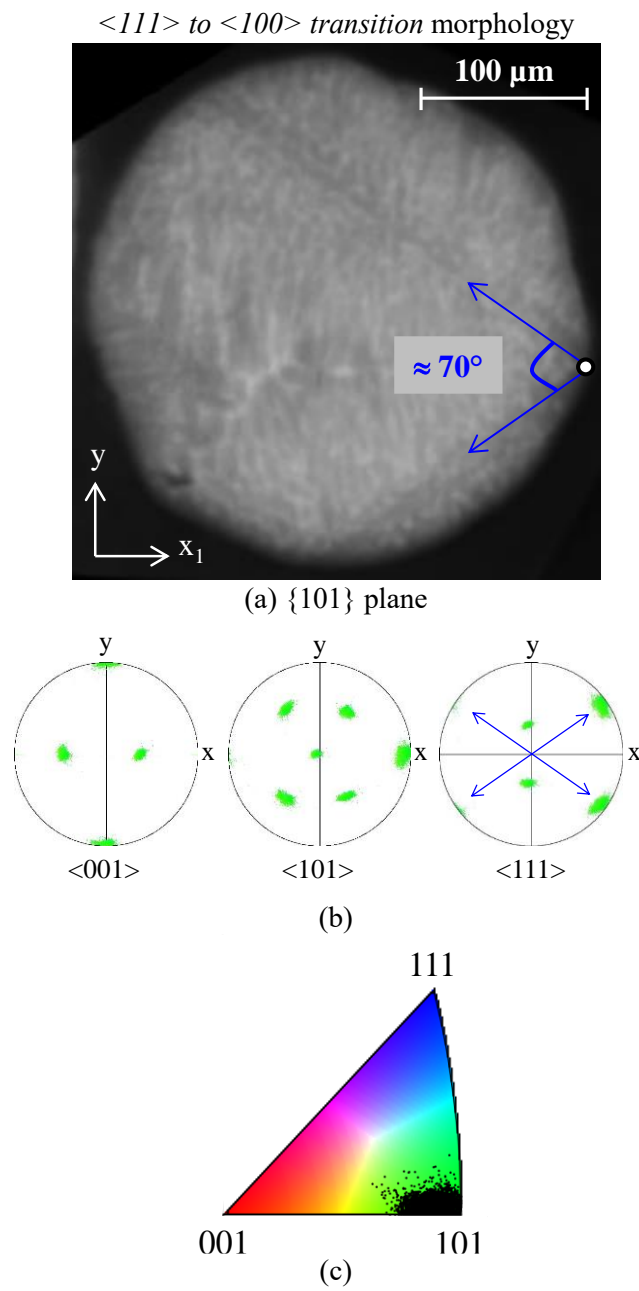


Figure 6. Tomography and EBSD analysis of the $\{101\}$ cross section represented in green in Figure 5, shown in (a). The two $\langle 111 \rangle$ primary arms are highlighted by blue arrows and the nucleation center by a white dot. The corresponding $\langle 001 \rangle$, $\langle 101 \rangle$ and $\langle 111 \rangle$ pole figures are shown in (b) and the inverse pole figure in (c).

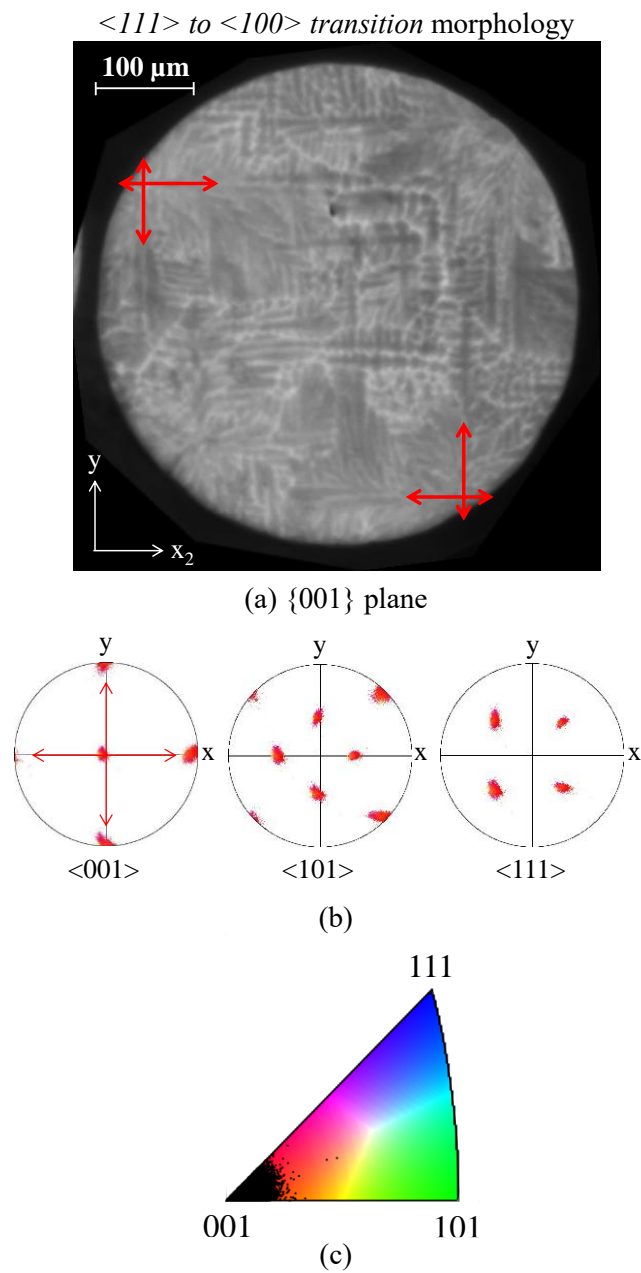


Figure 7. Tomography and EBSD analysis of the $\{001\}$ cross section represented in red in Figure 5, shown in (a). The corresponding $\langle 001 \rangle$, $\langle 101 \rangle$ and $\langle 111 \rangle$ pole figures are shown in (b) and the inverse pole figure in (c).

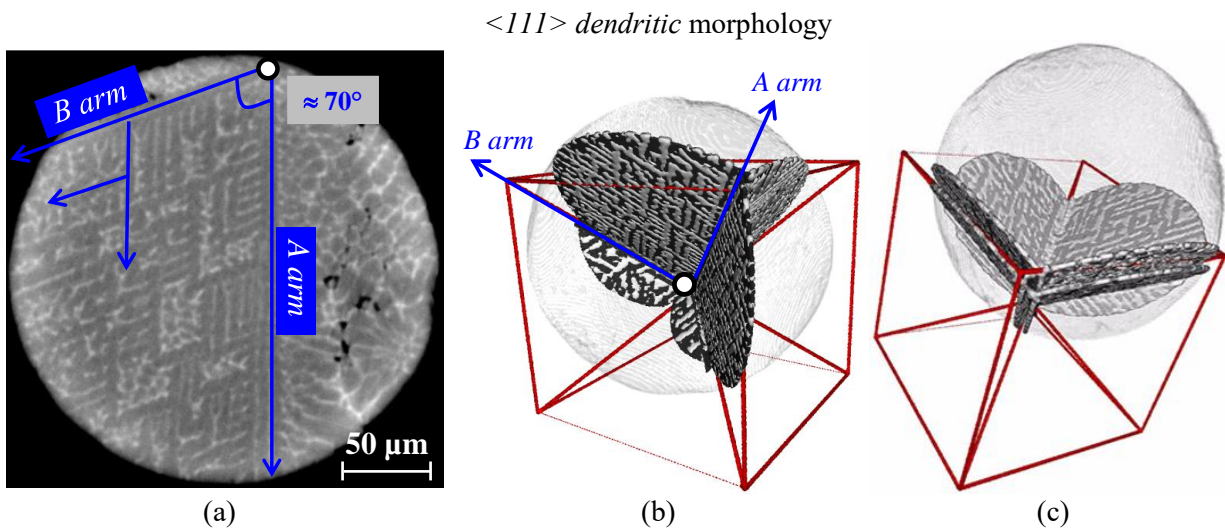


Figure 8. (a) Characteristic plane identified in a $255 \mu\text{m}$ diameter droplet solidified in argon, showing a dendritic morphology (arrows highlight primary arms *A arm* and *B arm*, secondary and tertiary dendritic arms), (b) the three-dimensional representation of the corresponding droplet with its surface in transparency, the dendritic planes in grey and the two primary arms *A arm* and *B arm* shown in (a) represented by blue arrows, and (c) the three-dimensional representation for a $244 \mu\text{m}$ diameter droplet solidified in argon, showing a dendritic morphology with double planes. In the three-dimensional representations, the droplets are placed in a cube with the nucleation center at the cube center and the primary arms towards the cube diagonals, illustrating the $\langle 111 \rangle$ growth orientation of the microstructure.

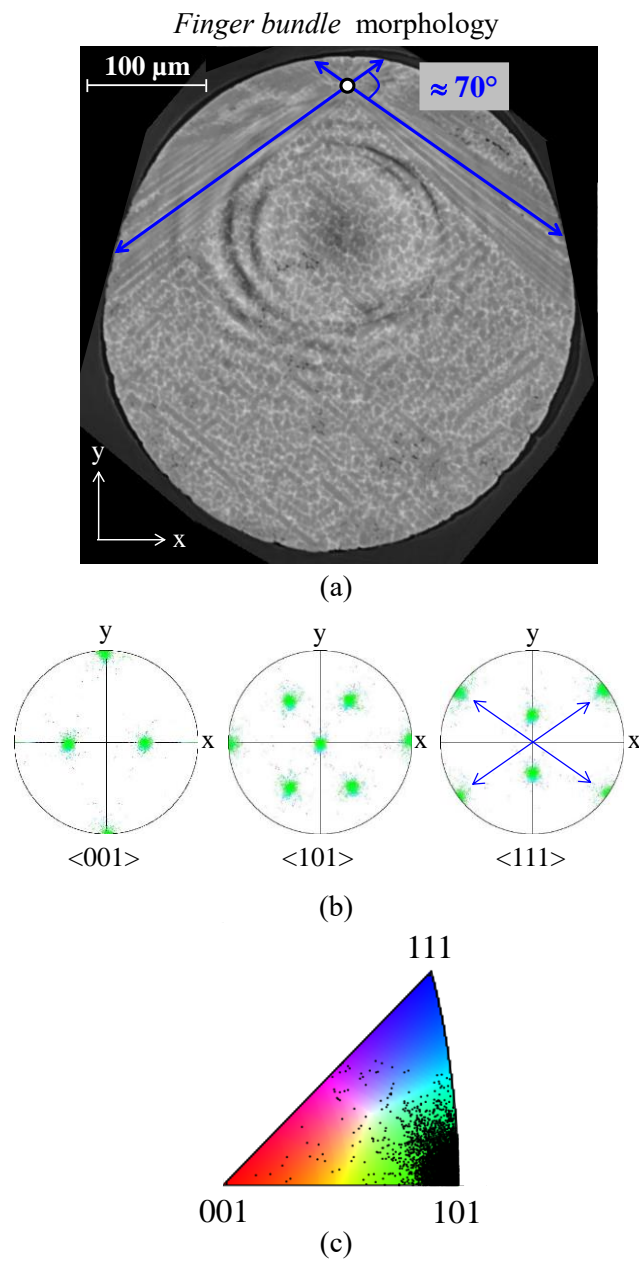


Figure 9. (a) Characteristic plane found in the tomography 3D-reconstruction of a 415 μm diameter droplet solidified in helium showing a finger-bundle structure. The two primary directions are highlighted by blue arrows and the nucleation center by a white dot. EBSD analysis provides the corresponding $\langle 001 \rangle$, $\langle 101 \rangle$ and $\langle 111 \rangle$ pole figures (b) and the inverse pole figure (c). The concentric black and white rings correspond to reconstruction artifacts that could not be corrected.

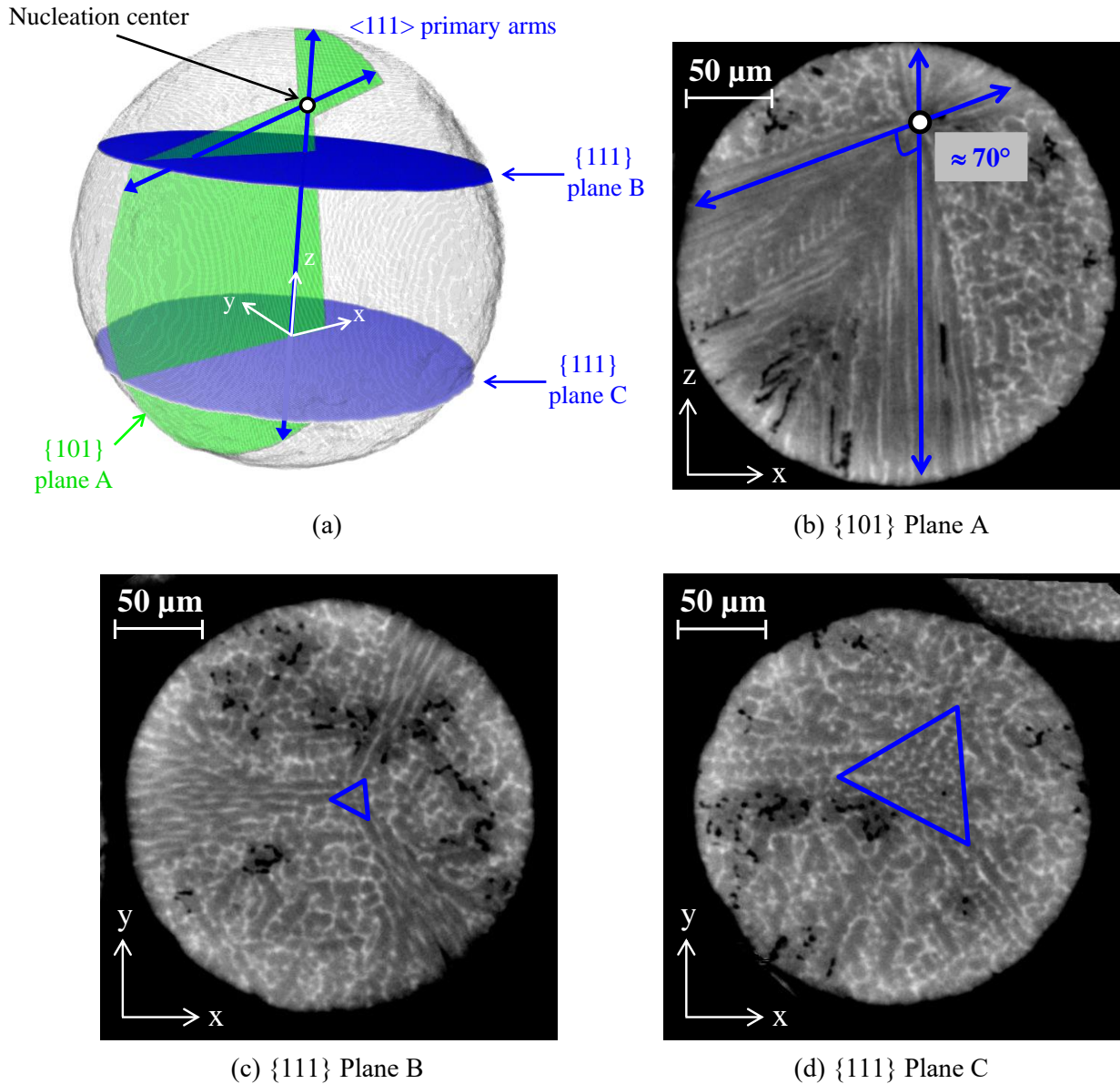


Figure 10. Widening of the finger bundle towards one $\langle 111 \rangle$ direction in a $264 \mu\text{m}$ diameter finger-bundle droplet solidified in argon. (a) Three-dimensional schematic view of the droplet with two $\langle 111 \rangle$ primary arms directions given by the blue arrows, the plane A containing those two primary directions in green, two planes orthogonal to a $\langle 111 \rangle$ direction Plane B and Plane C in blue and the nucleation center by the white dot. (b) Microstructure observed in plane A containing the two $\langle 111 \rangle$ directions. (c) Microstructure observed in Plane B, orthogonal to a $\langle 111 \rangle$ direction and close to the nucleation center. (d) Microstructure observed in Plane C, orthogonal to a $\langle 111 \rangle$ direction and far from the nucleation center. The blue triangles highlight the widening of the finger bundle when getting away from the nucleation center.

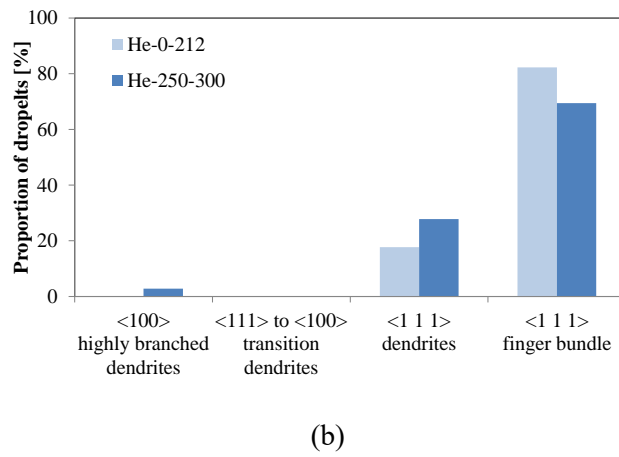
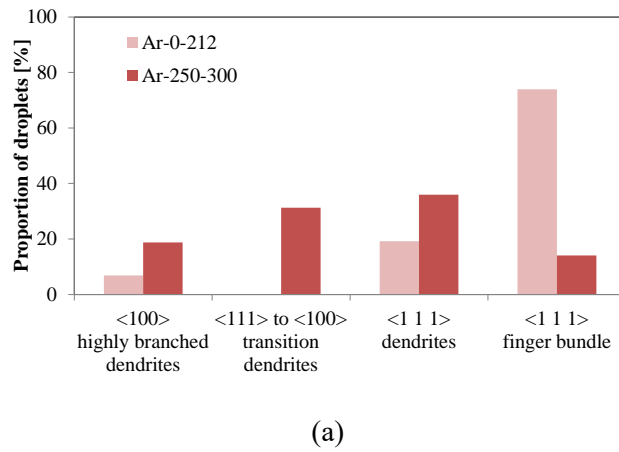


Figure 11. Distribution of the four observed morphologies in the droplets for two diameter ranges ($0 < d < 212 \mu\text{m}$ and $250 \mu\text{m} < d < 300 \mu\text{m}$) solidified in (a) argon and (b) helium.